PAPER

Check for updates

Insights from density functional theory calculations into the effects of the adsorption and dissociation of water on the surface properties of zinc diphosphide (ZnP₂) nanocrystals

Barbara Farkaš, [ID] [a] Aleksandar Živković, [ID] [ab] Veikko Uahengo,[c] Nelson Y. Dzade [ID] *[ad] and Nora H. de Leeuw [ID] [abe]

Zinc phosphides (ZnP₂ and Zn₃P₂) are emerging absorber materials for photovoltaic applications owing to their abundancy and non-toxic nature. Herein, we provide a comprehensive characterisation of the surface structure, composition, stabilities, morphology, and electronic properties of both bare and hydrated/hydroxylated low-Miller index surfaces of β-ZnP₂ by means of density functional theory (DFT) calculations. Mechanistic insights into the fundamental aspects of water adsorption and dissociation, including the adsorption geometries, energetics, and structural parameters along the reaction path are systematically characterised. The stabilities of the surfaces under dry and wet conditions are discussed in detail and the predicted phase diagrams for the water adsorption are presented. Using calculated surface energies, we have derived the equilibrium morphology of the β-ZnP₂ nanocrystals under vacuum and upon hydration or hydroxylation. Atomic-level insights into the origin of the incipient oxidation of β-ZnP₂ surfaces are provided through analysis of Bader charges, which reveal that the Zn sites to which H₂O and OH species are bound undergo oxidation due to the transfer of charge to the adsorbed species. Adsorption-induced changes to the electronic properties before and after hydration/hydroxylation were characterised by the work function and partial density of states. The results highlight the need for protection of β-ZnP₂ nanocrystals against possible oxidation in the presence of water through post-synthesis organic functionalisation.

Introduction

Significant interest in inorganic semiconductors as absorber materials for third-generation solar cells has been triggered by their potential to overcome the challenges of availability, high-cost processing, and toxicity, which have been insurmountable for the highly efficient first- and second-generation photovoltaics.[1–3] Moreover, extensive tuning possibilities of their optoelectronic properties are providing a counterbalance between these advantageous characteristics and their lower energy conversion performance, making these materials promising candidates in the renewable energy field.[4–6] The pursuit of non-toxic and Earth-abundant precursors for solar absorber materials has influenced extensive efforts in the development of II–VI (copper, zinc, and iron sulphides and oxides) and III–V (indium and gallium phosphides) compounds for photovoltaic (PV) purposes.[7–11] Despite the intensive research focus on these materials, PV devices with efficient power conversion have not yet been demonstrated, which necessitates the development of new solar absorber materials with increased efficacy.

From a recent cost-benefit analysis performed on a number of Earth-abundant semiconducting materials, zinc phosphides have been proposed to be among the most promising materials for large-scale PV applications with a significant cost-reduction over crystalline silicon.[12] Tetragonal Zn₃P₂ has recently seen a resurgence of interest for cost-effective and scalable thin-film PV devices, owing to its direct bandgap of 1.5 eV,[13] high visible-light absorption coefficient ($>10^4$ cm⁻¹),[14] long minority-carrier diffusion length ($\sim$10 µm),[15] high extinction coefficient,[16] and large range of potential doping concentrations (10^{13}–10^{18} cm⁻³).[17] Zinc diphosphide (ZnP₂), which crystallizes in two distinct polymorphs, the tetragonal α-ZnP₂ (red) and monoclinic β-ZnP₂ (black), has, on the other hand, received limited attention for

a School of Chemistry, Cardiff University, Main Building, Park Place, Cardiff, CF10 3AT, UK

b Department of Earth Sciences, Utrecht University, Princetonlaan 8a, 3548CB Utrecht, The Netherlands

c Department of Chemistry and Biochemistry, University of Namibia, 340 Mandume Ndemufayo Avenue, Windhoek 9000, Namibia

d Department of Energy and Mineral Engineering, Pennsylvania State University, University Park, PA 16802, USA. E-mail: nxd5313@psu.edu

e School of Chemistry, University of Leeds, Leeds LS2 9JT, UK

PV applications. The α-ZnP$_2$ phase is characterized by a 2.10–2.30 eV indirect and dipole forbidden bandgap,[18–20] while the β-ZnP$_2$ phase has a direct bandgap of 1.30–1.61 eV, which is ideally suited for efficient light absorption.[20–22] Based on the power-production predictions, it is estimated that β-ZnP$_2$ could potentially facilitate a 3.5×10^5 and 2.0×10^4 times increased PV production compared to InP and GaAs, respectively, in a cell operating at 10% efficiency.[23] In our recent study, we have employed the screened hybrid approach to determine the optoelectronic and dielectric properties of the α-ZnP$_2$ and β-ZnP$_2$ phases, and predicted a thin-film PV absorbing efficiency of almost 10% for β-ZnP$_2$.[24]

As surfaces and interfaces play an important role in the rational design of tandem solar cells, it is important to gain an atomic-level understanding of their structures and composition, whereas the relative stabilities of β-ZnP$_2$ surfaces and possible changes in their electronic structures and crystal morphology upon prolonged exposure to wet conditions should also be elucidated for practical applications. Low surface stability in the presence of moisture and oxygen[10,11] remains a major problem that severely limits commercial fabrication of efficient zinc-based PV materials.[25–29] Under working conditions, the presence of adsorbed water leads to surface hydration, thereby modifying the stability of the exposed facets. The adsorbed water molecules can also modulate the electronic properties of the surface by shifting the positions of the valence band maximum and conduction band minimum, which could greatly affect the light absorption capacity. Detailed quantitative assessment of the changes that originate from the presence of water at working conditions is thus crucial for the realistic evaluation of the suitability of a material for PV applications, and could indicate a need for further protection of the surfaces.

In this work we have systematically characterised the structure, composition, morphology, and electronic properties of both clean and hydrated/hydroxylated low-Miller index surfaces of β-ZnP$_2$ by means of density functional theory calculations and, in conjunction with the *ab initio* thermodynamics, we have investigated the behaviour of the surfaces in humid environment. The atomic-level description of water adsorption, induced electronic effects, and changes in the stability of the surfaces under dry and wet conditions are discussed in detail and the predicted phase diagrams for the water adsorption are presented. Using the calculated surface energies, we have derived the equilibrium morphology of the β-ZnP$_2$ nanocrystals upon hydration and hydroxylation of the relevant surfaces.

Computational details

The spin-polarised calculations with the projector augmented wave (PAW)[30,31] pseudo-potential method have been carried out within the usual Kohn–Sham (KS) implementation of density functional theory (DFT)[32,33] using the Vienna ab initio Simulation Package (VASP).[34] The generalised gradient approximation (GGA) was employed to approximate the exchange–correlation functional using parametrisation developed by

Perdew–Burke–Ernzerhof (PBE).[35] The core electrons up to and including the 3p, 2p, and 1s levels of Zn, P, and O, respectively, were kept frozen with the long-range dispersion interactions added through the Grimme DFT-D3 method.[36] Bulk calculations were carried out in the reciprocal space with a $5 \times 5 \times 5$ k-point mesh, and the kinetic energy cut-off of the wave function was set to 500 eV. The METADISE code,[37] which ensures the creation of surfaces with zero dipole moment perpendicular to the surface plane, was employed to construct the structures of the seven low-Miller index surfaces of β-ZnP$_2$: (001), (010), (011), (100), (101), (110), and (111). The surface models were built as slabs of material, comprising 12 atomic layers (four ZnP–P–ZnP trilayers each containing four ZnP$_2$ units), with periodic boundary conditions and a 15 Å vacuum which was added in the direction orthogonal to the surface to prevent interactions between periodic images. All atoms in the slab were allowed to relax unconstrainedly until residual forces on all atoms had reached 10^{-3} eV Å^{-1}. The conjugate gradient technique, with total energy and force convergence criteria of 10^{-6} eV and 0.01 eV Å^{-1}, respectively, has been used to perform structural optimisations.

Surface energies, γ, have been calculated as a measure of the thermodynamic stability using the relation:

$$\gamma = \frac{E_{\text{surface}}^{\text{DFT}} - n \times E_{\text{bulk}}^{\text{DFT}}}{2A_{\text{surface}}}, \qquad (1)$$

where γ represents the surface energy, $E_{\text{surface}}^{\text{DFT}}$ and $E_{\text{bulk}}^{\text{DFT}}$ are the total energies (per unit cell) of relaxed surface slab and bulk systems, respectively, A_{surface} is the surface area, and n is the ratio between the number of atoms in the slab and the number of atoms in the bulk. The surface with the lowest surface energy is predicted to be the most stable. Based on the calculated surface energies, the equilibrium Wulff morphology[38] for the β-ZnP$_2$ nanocrystal was constructed using the Wulffmaker[39] software.

Adsorption of molecular and dissociated water was carried out on all seven low-Miller index surfaces of β-ZnP$_2$ to determine the effect of hydration/hydroxylation on surface stabilities, electronic properties, and crystal morphology. Water molecules and OH/H fragments were positioned 2 Å above the top surface layer in varying adsorption positions, and both adsorbates and slab atoms were then allowed to relax without any constrains. 1×1 cells were found to be sufficiently large to prevent interaction of periodic images of the adsorbates, providing an average of 7.5 Å distance between them on all seven low-Miller index surfaces. Adsorption was carried out on one facet only, employing the dipole correction in the orthogonal direction. The adsorption energy, E_{ads}, which quantifies the strength of adsorption, was calculated as:

$$E_{\text{ads},m\text{H}_2\text{O/OH}-\text{H}} = \frac{1}{m}\left[E_{\text{surface}+m\text{H}_2\text{O/OH}-\text{H}}^{\text{DFT}} - \left(E_{\text{surface}}^{\text{DFT}} + m \times E_{\text{H}_2\text{O}}^{\text{DFT}}\right)\right] \qquad (2)$$

where $E_{\text{surface}+m\text{H}_2\text{O/OH}-\text{H}}^{\text{DFT}}$, $E_{\text{surface}}^{\text{DFT}}$, and $E_{\text{H}_2\text{O}}^{\text{DFT}}$ are the total energies (per unit cell) of the system comprising of the surface slab with m adsorbed water molecules or OH/H fragments, the

relaxed surface slab, and the water molecule, respectively. The latter was determined by optimising a single water molecule in a cubic box of 15 Å each side, sampling only the gamma point. A negative adsorption energy represents exothermic and spontaneous reaction. The work function (ϕ) of the surfaces before and after hydration/hydroxylation was calculated as the difference between the vacuum electrostatic potential energy, E_{vac}, and the energy of the Fermi level, E_F.

The effects of increased water coverage (coverage in ML = $m_{H_2O}/n_{Zn\text{-under-coordinated}}$) have also been investigated by increasing the number of adsorbed water molecules until all under-coordinated metallic sites were saturated (m_{H_2O} = $n_{Zn\text{-under-coordinated}}$), which was considered to be full a monolayer coverage, 1.00 ML. In the case of hydroxylation, 1.00 ML corresponds to the saturation of under-coordinated surface zinc ions with OH fragments ($m_{OH} = n_{Zn\text{-under-coordinated}}$). Considering that the surface energies of hydrated/hydroxylated surfaces differ from unhydrated surface energies (eqn (1)) by the factor which depends on the energy released upon the adsorption (eqn (2)), thereby altering the equilibrium crystal morphology, the hydrated/hydroxylated surface energies were also calculated. After the molecular or dissociated adsorption of water, the surface energies of the fully hydrated/hydroxylated β-ZnP$_2$ surfaces, γ_h, were calculated as:

$$\gamma_h = \gamma + m \times \frac{E_{ads,mH_2O/OH-H}}{2A_{surface}}$$

$$= \frac{E_{surface+mH_2O/OH-H}^{DFT} - \left(n \times E_{bulk}^{DFT} + m \times E_{H_2O}^{DFT} \right)}{2A_{surface}}. \quad (3)$$

The thermodynamics of surfaces with different water coverages in equilibrium with a water reservoir was introduced by comparing the surface free energy of the hydrated/hydroxylated surfaces, σ_h:

$$\sigma_h(T,p) = \sigma_h(0\ K) + \sigma_h(T,p). \quad (4)$$

The surface free energy σ is a Gibbs free energy needed to create the specific surface structure per surface area, with bulk and gas phase components taken as reference points for the adsorbing material and the adsorbate, respectively. Hence $\sigma_h(0\ K) = \gamma_h$, and thermodynamic (T, p) conditions are introduced through the chemical potentials of constituting elements:

$$\sigma_h(T,p) = \frac{1}{A_{surface}}\left[G_{surface+mH_2O} - n_{ZnP_2}\mu_{ZnP_2}(T,p) - m\mu_{H_2O}(T,p) \right]$$

$$(5)$$

$$\Delta\sigma_h(T,p) =$$

$$\frac{1}{A_{surface}}\left[G_{surface+mH_2O} - G_{surface} - \Delta n_{ZnP_2}\mu_{ZnP_2}(T,p) - \Delta m\mu_{H_2O}(T,p) \right]$$

$$(6)$$

where $G_{surface}$ is the free energy of the surface, $G_{surface+mH_2O}$ is the free energy of the system comprising n ZnP$_2$ units and m adsorbed water molecules, and μ_{ZnP_2} and μ_{H_2O} are ZnP$_2$ and H$_2$O chemical potentials. Since the surface slab models where not changed throughout the adsorption process, the number of ZnP$_2$ units is a constant ($\Delta n_{ZnP_2} = 0$), and (T,p) dependence is introduced solely through μ_{H_2O}:

$$\mu_{H_2O}(T,p) = \left[G_{H_2O} + \Delta g_{H_2O}(T,p_0) + k_B T \ln\left(\frac{p_{H_2O}}{p_0} \right) \right] \quad (7)$$

where p_0 is the atmospheric pressure, and $g_{H_2O}(T,p_0)$ is the change in the Gibbs energy of water between 0 K and T at p_0 (extracted from thermodynamic tables[40]). The final term represents the change in the energy p_0 and p_{H_2O} at T. Using these expressions, Gibbs free energies of systems with varying water coverages are reported as a function of μ_{H_2O} in form of surface phase diagrams.

Results and discussion

Bulk and surface characterisation of β-ZnP$_2$

The lattice parameters of the monoclinic β-ZnP$_2$ structure (Fig. 1a) are predicted at a = 8.611 Å, b = 7.239 Å, and c = 7.530 Å, in close agreement with experimental reports and
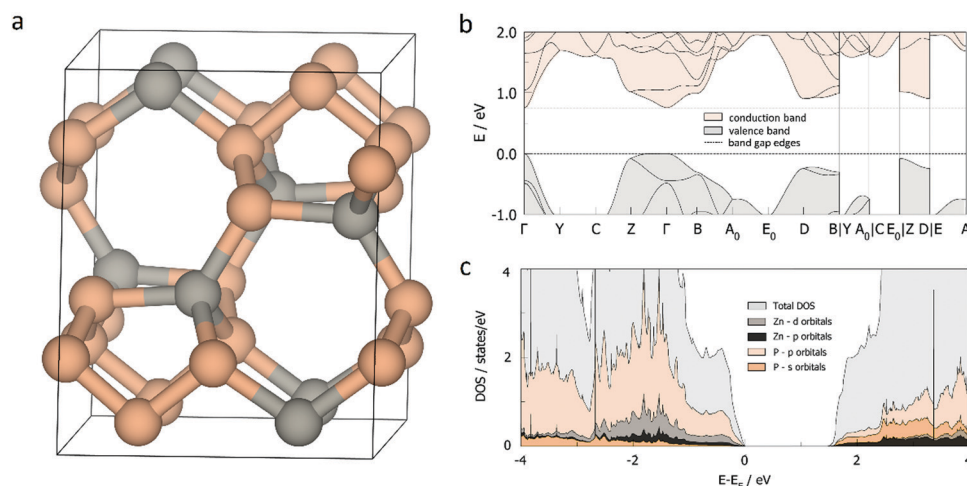

Fig. 1 (a) GGA optimised bulk structure; (b) HSE06 calculated band structure; and (c) HSE06 calculated projected densities of state (DOS) of monoclinic β-ZnP$_2$.

previous theoretical results.[20,41–45] The electronic band structure (Fig. 1b), with the band gap calculated as a 1.46 eV direct transition, in correspondence with the experimentally reported range of 1.33–1.60 eV,[42,46–48] and features of the partial density of states, DOS (Fig. 1c), were well reproduced in our previous study[49] using the HSE06 hybrid functional compared to the severely underestimated values of other published DFT results. The valence band of β-ZnP$_2$ is found to be dominated by the electronic states of the Zn-pd and P-p orbitals, whereas the conduction band is composed mainly of the Zn-d orbitals.[24] The relaxed bulk β-ZnP$_2$ structure was employed to create the seven low-Miller index surfaces – (001), (010), (100), (011), (101), (110) and (111) – and considering all possible non-dipolar terminations. Each surface was fully relaxed to predict the lowest-energy structures, surface energies, and order of stability. The most stable termination for each surface is represented in top and side view in Fig. 2, whereas their terminations, calculated surface energies and extent of relaxations are summarised in Table 1.

The (001) and (011) surfaces are predicted to be the most stable surfaces of β-ZnP$_2$ with calculated surface energies of 0.728 and 0.739 J m^{-2}, respectively. The surface energies of the (010), (100), (101), (110) and (111) surface are calculated in order at 0.949, 0.889, 0.899, 1.028, and 0.985 J m^{-2}. These results suggest that a surface stability trend in decreasing order of (001) > (011) > (100) > (101) > (010) > (111) > (110). As reflected in the calculated percentage relaxation (Table 1), each surface is found to undergo significant relaxation, ascribed to the adjustments of the topmost under-coordinated ions, which shift downward to provide a closer-to-bulk coordination of the surface species. Observed inward relaxation of the surface planes does not exceed a few percent, whereas a more pronounced rumpling of the under-coordinated surface Zn atoms from 2.15 to 8.05% was captured, accounting for 10–15% of the spacing between the pairs of Zn ions in different surface trilayers. Overall, the bulk-ward displacement of the top-most ions occurred to a higher extent for Zn ions, whereas the position of surface P ions remained relatively unchanged, with movements of less than 2.0%. More significant reconstructions of surface layers were not achieved through the surface relaxation.

Table 1   The most stable terminations for seven low-Miller index surfaces of β-ZnP$_2$ with accompanying unrelaxed and relaxed surface energies (γ_u and γ_r), and overall rate of relaxation in %

	Termination	γ_u/J m^{-2}	γ_r/J m^{-2}	Relaxation/%
(001)	–Zn–Zn–	1.006	0.728	−27.63
(010)	–P–P–	1.278	0.949	−25.74
(100)	–P–Zn–	1.514	0.889	−41.28
(011)	–Zn–	1.001	0.739	−26.17
(101)	–P–P–	1.165	0.899	−22.83
(110)	–P–	1.699	1.028	−39.49
(111)	–Zn–	1.364	0.985	−27.79

Molecular adsorption of water on β-ZnP$_2$ surfaces

The adsorption of water molecules on β-ZnP$_2$ surfaces represents an important step in their oxidation process. Therefore, the aim of this work is to determine the lowest-energy geometries for water adsorption and changes in the surface properties induced upon hydration or hydroxylation. Prior to the investigation of complete surface hydration, where all surface cation sites are terminated by a water molecule, the adsorption geometries (Fig. 3) and energetics (Table 2) of single water molecule adsorption on each surface were systematically characterised. Placement of water molecules in different positions above the surfaces has always led to their coordination through the oxygen to one of the available Zn surface ions, and hence all distinct surface Zn atoms were considered to determine the preferred adsorption binding site for water molecule. The square geometry of the (001) surface provides the same environment for both of the under-coordinated Zn atoms, and hence it has only one possible adsorption site. The remaining surfaces are characterised by rhomboid, channel-like arrangements and consequently have two different types of under-coordinated Zn adsorption sites. The first site, denoted here as Zn$_{in-plane}$, provides a flat adsorption with the water molecule positioned completely above the surface or at the level of the topmost surface atoms; the second site, Zn$_{channel}$, lies further down in the surface's channel and allows the incorporation of the water molecule within the channel. For the more closely packed (110) and (111) surfaces, the distinction between the 'flat' in-plane and built-in channel adsorption sites is much less pronounced, owing to the minimal difference in the z-direction positioning of the surface Zn cations.
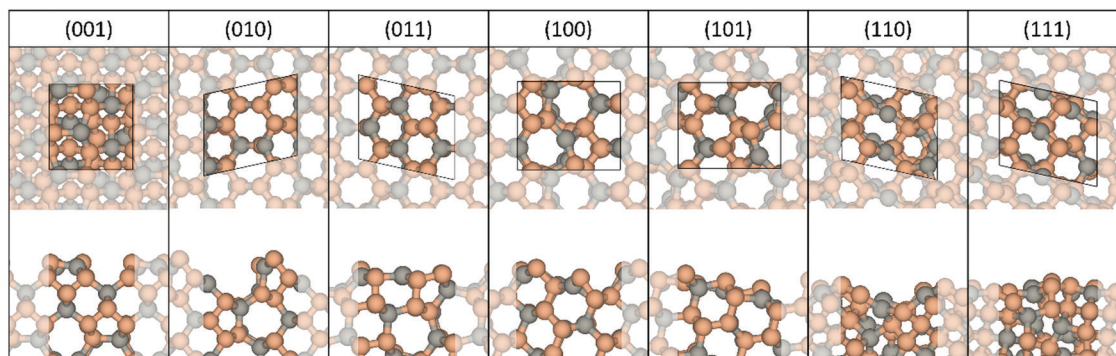
Fig. 2   Top and side views of the most stable terminations of seven low-Miller index surfaces of β-ZnP$_2$. Atomic colour: Zn in grey, and P in peach.
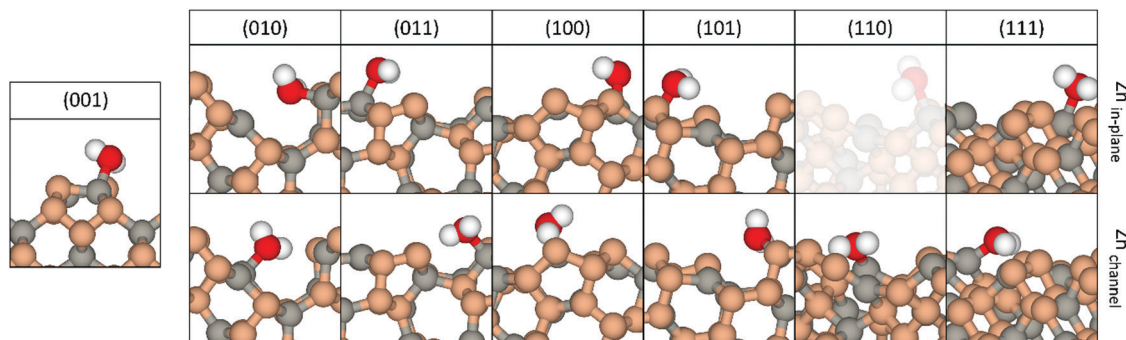
Fig. 3 Side views of single water molecule adsorption at different Zn binding sites on the low-Miller index surfaces of β-ZnP$_2$. The (001) surface has only one unique Zn adsorption site. The Zn$_{in-plane}$ adsorption on the (110) surface resulted in the spontaneous rearrangement and is hence shown in faded colours. Atomic colour: Zn in grey, P in peach, O in red, and H in white.

Table 2 Energies of adsorption (per water molecule), E_{ads,mH_2O}, from single water molecule to a full monolayer adsorbed on seven low-Miller index surfaces of β-ZnP$_2$ with accompanying zinc-oxygen distances (d_{Zn-O}), hydrated surface energies (γ_h) and relaxation rates in %

	mH$_2$O	E_{ads,mH_2O}/eV	d_{Zn-O}/	γ_h/J m^{-2}	Relaxation upon hydration/%
(001)	1 (Zn$_{in-plane}$)	−0.769	2.230	0.615	−15.52
	2	−0.658	2.288, 2.266	0.534	−26.65
(010)	1 (Zn$_{in-plane}$)	−0.744	2.315	0.857	−9.69
	1 (Zn$_{channel}$)	−0.957	2.186	0.831	−12.43
	2	−0.803	2.147, 2.344	0.751	−20.86
(100)	1 (Zn$_{in-plane}$)	−0.609	2.258	0.813	−8.55
	1 (Zn$_{channel}$)	−0.680	2.259	0.804	−9.56
	2	−0.604	2.284, 2.289	0.738	−16.99
(011)	1 (Zn$_{in-plane}$)	−0.635	2.287	0.679	−8.12
	1 (Zn$_{channel}$)	−0.910	2.166	0.653	−11.64
	2	−0.752	2.179, 2.296	0.597	−17.91
(101)	1 (Zn$_{in-plane}$)	−0.701	2.207	0.838	−6.79
	1 (Zn$_{channel}$)	−0.779	2.205	0.831	−7.56
	2	−0.718	2.227, 2.228	0.774	−13.90
(110)	1 (Zn$_{channel}$)	−0.952	2.097	0.944	−8.17
	2	−0.843	2.111, 2.213	0.879	−14.49
(111)	1 (Zn$_{in-plane}$)	−0.665	2.240	0.938	−4.77
	1 (Zn$_{channel}$)	−0.961	2.139	0.917	−6.90
	2	−0.824	2.132, 2.237	0.868	−11.88
	3	−0.735	2.147, 2.236, 2.298	0.829	−15.84

At the (001) surface, the adsorption energy of a single water molecule is calculated to be −0.769 eV, with an O–Zn bond distance of 2.230 Å. A similar adsorption energy of −0.744 eV is released at the Zn$_{in-plane}$ site on the (010) surface, whereas the interaction is stronger when water binds to the Zn$_{channel}$ with an E_{ads} of −0.957 eV. The interacting O–Zn distances are predicted at 2.315 Å and 2.186 Å at Zn$_{in-plane}$ and Zn$_{channel}$ sites, respectively. At the (100) surface, the calculated adsorption energies of a single water molecule adsorption in the Zn$_{in-plane}$ and Zn$_{channel}$ sites are −0.609 and −0.680 eV, respectively, with almost identical O–Zn bond lengths of 2.258 and 2.259 Å, due to the very shallow surface channels. Together with the (011) Zn$_{in-plane}$ adsorption energy of −0.635 eV at an oxygen–zinc distance of 2.287 Å, the binding strengths of both adsorption sites on the (100) surface are the lowest observed, especially amongst the channel-incorporated adsorbate molecules. Adsorption of water in the Zn$_{channel}$ site of the (011) surface with an adsorption energy of −0.910 eV was shown to be significantly stronger (Δ = 0.275 eV) than in the Zn$_{in-plane}$ site.

For the Zn$_{in-plane}$ and Zn$_{channel}$ sites of the (101) surface, the adsorption of a single water molecule released respective energies of 0.701 and 0.779 eV. Finally, the more closely packed (110) and (111) surfaces show the most favourable water adsorption. At the (110) surface, the water molecule initially positioned to bind at the Zn$_{in-plane}$ site (shown in faded colours in Fig. 3) spontaneously moved to the Zn$_{channel}$ surface atom, where the adsorption energy was calculated to be −0.952 eV at the shortest captured O–Zn distance of the investigated systems, 2.097 Å. The strongest adsorption, −0.961 eV, was established for the Zn$_{channel}$ site of the (111) surface, 0.296 eV more favourable than when binding to the Zn$_{in-plane}$ atom, which is also the largest calculated difference between the distinct adsorption sites. The interacting O–Zn bond distance is found to generally indicate the strength of water adsorption: the shorter the O–Zn bond, the stronger the adsorption.

Having characterised the geometries and energetics of the adsorption of a single water molecule on each surface, the number of water molecules was progressively increased until all
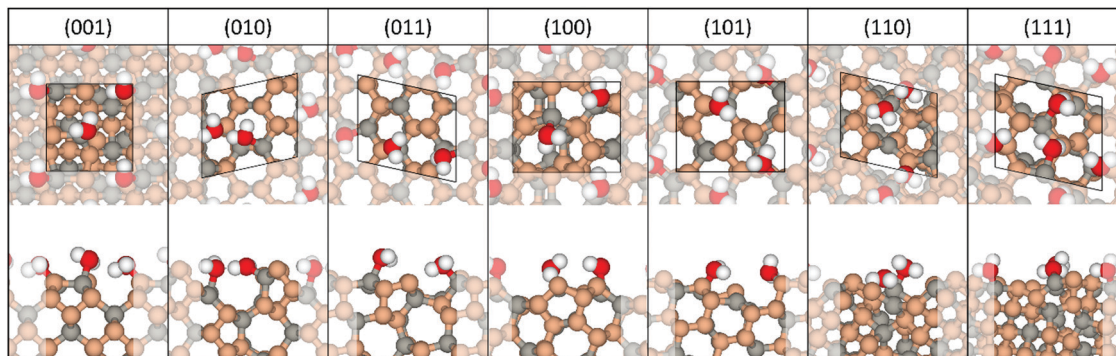
26486 | *Phys. Chem. Chem. Phys.*, 2021, **23**, 26482–26493

This journal is © the Owner Societies 2021

Fig. 4 Top and side views of low-Miller index surfaces of β-ZnP$_2$ with a full coverage of water after molecular adsorption (hydration). Atomic colour: Zn in grey, P in peach, O in red, and H in white.

surface Zn cation sites were terminated by water, which was considered to be a full monolayer coverage. The number of molecules needed to achieve full coverage differs from surface to surface, as represented in the top and side views of the optimised structures in Fig. 4. The (001), (010), (100), (011), (101), and (110) surface simulation cells can each accommodate two water molecules, whereas three molecules are needed to saturate the cation sites of the (111) surface. The adsorption energies per water molecule for monolayer coverages are summarized in Table 2, together with the relaxed surface energies and corresponding structural parameters.

The adsorption energies per water molecule for monolayer coverage (2 water molecules per surface) on the (001) and (100) surfaces are the smallest amongst the seven systems, calculated at −0.658 and −0.604 eV, respectively, followed by the slightly stronger interactions of −0.752 and −0.718 eV established on the (011) and (101) surfaces. The (010) and (110) surfaces showed even stronger adsorption with adsorption energies calculated to be −0.803 and −0.843 eV per molecule, respectively. Adsorption of two water molecules to form a hydration monolayer on the (110) surface always resulted in the relaxation of both water molecules to coordinate the same channel Zn site, releasing a significant adsorption energy per molecule and leaving the Zn$_{in-plane}$ atom without any adsorbate interactions. Even the

addition of a third water molecule did not change this pattern, as it is accommodated to form hydrogen-bonds with the two co-adsorbed water molecules instead of binding at the available Zn$_{in-plane}$ site. Finally, adsorption of two water molecules on the (111) surface yielded an adsorption energy of −0.824 eV per water molecule. However, up to three water molecules can bind to the (111) surface to form a monolayer, which released an adsorption energy of −0.735 eV per water molecule. The average adsorption energy at each surface is found to decrease with the increasing number of water molecules. For instance, on the (111) surface, the adsorption energy decreased from −0.961 eV calculated for the adsorption of a single water molecule to −0.824 and −0.735 eV obtained for two and three adsorbed water molecules, respectively.

Molecular water adsorption induced changes in the surface structures, and their post-hydration stabilities were characterised by calculating the hydrated surface energies and percentage of relaxation after water adsorption, Table 2. The stability order of the seven surfaces after single water adsorption remained the same as for the unhydrated surfaces, with the exception of the (010) and (101) surfaces which have the same hydrated surface energies. Upon full monolayer adsorption, the stability of the (010) surface exceeds that of the (101) surface by 0.023 J m^{-2}, slightly modifying the stability order. All of the
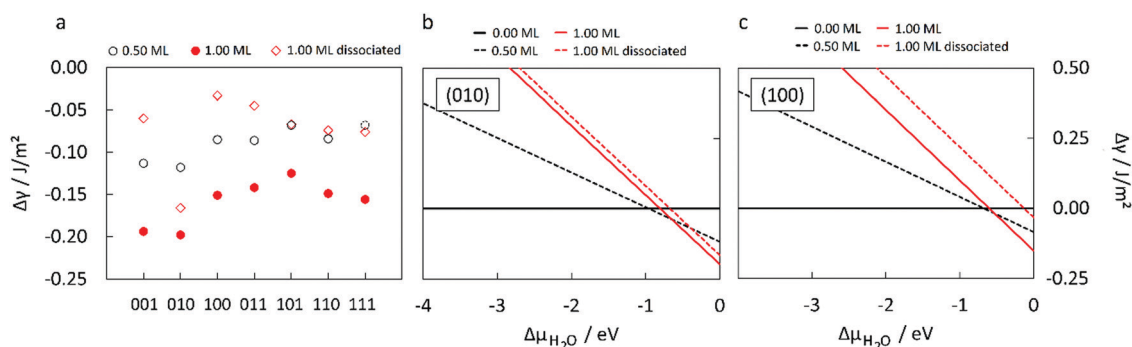

Fig. 5 (a) Changes in the surface energy for seven low-Miller index surfaces of β-ZnP$_2$ induced by a half and full monolayer hydration and a full monolayer hydroxylation at 0 K. Because the (111) surface can accommodate three water molecules to form a full monolayer, the respective data point for lower coverage corresponds to a 0.33 ML and is hence shown in dashed border lines. (b) Changes in the surface energy of the (010) surface with respect to the chemical potential of water. (c) Changes in the surface energy of the (100) surface with respect to the chemical potential of water.

This journal is © the Owner Societies 2021

Phys. Chem. Chem. Phys., 2021, **23**, 26482–26493 | **26487**

surfaces have experienced a certain level of stabilisation (between 14 and 27%) as their surface energies were lowered once covered by water monolayers. The stabilisation of the surfaces upon full monolayer hydration can be rationalised by considering the fact that the water molecules bind to the under-coordinated Zn cations, providing a closer match to the bulk coordination of the surface Zn species.

Changes in the surface energies upon half and full mono-layer hydration, $\Delta\gamma_h$, have been captured in Fig. 5a. To gain insight into the effect of experimental conditions on the stabilities of the hydrated surfaces, the study of the change in the surface energies was extended to include the alternations induced by the chemical potential of water, $\Delta\mu_{H_2O}$, which has a built-in dependence on the temperature and pressure. This effect is shown for two surfaces, the (010) that experienced the highest rate of relaxation upon water adsorption (Fig. 5b) and the (100) representing the mid-average of all seven surfaces (Fig. 5c). The two surfaces show similar trends, with the hydration being favoured up to the chemical potential of water of -0.68 eV for the (100) surface and -0.96 eV for the (010) surface. A transition from the full monolayer to the half monolayer coverage is observed at -0.53 and -0.66 eV $\Delta\mu_{H_2O}$ potentials, respectively. In an environment with standard pressure and temperature conditions ($p = 1$ atm, $T = 300$ K), the partial pressures of water required for spontaneous hydra-tion of the β-ZnP$_s$ low-Miller index surfaces correspond to the relatively low values of $\sim 10^{-6}$–10^{-10} atm. Considering that the partial pressure of water vapour in the air is 5–48×10^{-3} atm in the 0–30 °C temperature range, water adsorption is very likely to take place on any of the β-ZnP$_2$ surfaces.

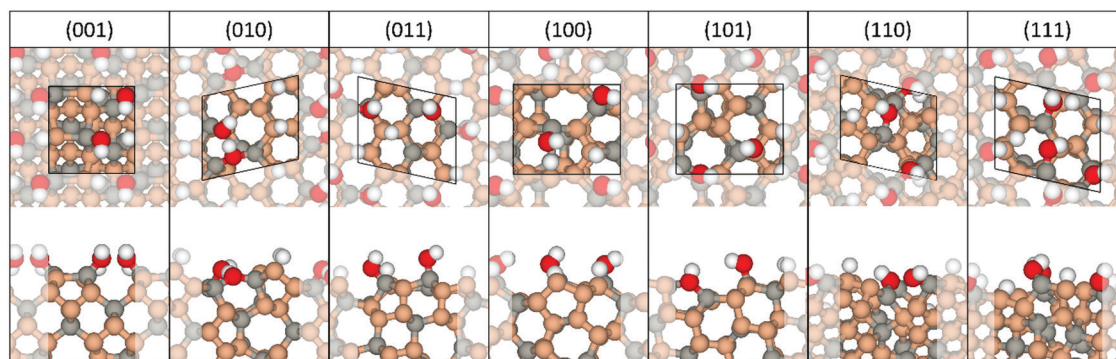### Dissociative adsorption of water on β-ZnP$_2$ surfaces

The adsorption of a fully dissociated monolayer of water and the effect of hydroxylation on the stabilisation of different β-ZnP$_2$ surfaces has also been investigated. Optimised disso-ciative water geometries are presented in Fig. 6, with structural and energetic parameters listed in Table 3. The OH fragment remained bound at the Zn adsorption site through a Zn–O bond, whereas the dissociated hydrogen atom moved to the available surface P sites. Generally, on all seven surfaces weaker adsorption energies were calculated for dissociated water

Table 3 Adsorption energies per molecule, E_{ads,mH_2O}, of fully dissociated monolayer of water adsorbed on seven low-Miller index surfaces of β-ZnP$_2$ with accompanying zinc–oxygen distances (d_{Zn-O}), hydroxylated surface energies (γ_h) and relaxation rates in %

	mH_2O	E_{ads,mH_2O}/eV	d_{Zn-O}/	γ_h/J m^{-2}	Relaxation upon hydration/%
(001)	2	-0.203	1.866, 1.867	0.668	-8.24
(010)	2	-0.672	1.935, 2.037	0.783	-17.49
(100)	2	-0.132	1.880, 1.880	0.856	-3.71
(011)	2	-0.239	1.863, 1.866	0.694	-6.09
(101)	2	-0.450	1.866, 1.863	0.832	-7.45
(110)	2	-0.421	2.143, 2.147	0.954	-7.20
(111)	3	-0.356	1.847, 2.020, 1.894	0.909	-7.72

adsorption (Table 3) compared to those obtained for the adsorption of water in the molecular state (Table 2). For example, the average dissociative adsorption energy per water molecule for two adsorbed molecules on the (001) surface is calculated at -0.203 eV, which is significantly weaker than the adsorption energy of -0.658 eV calculated for molecular adsorption of a full monolayer.

The most pronounced difference between the two adsorp-tion states of water molecules was observed on the (100) surface, where molecular adsorption released 0.472 eV more energy per water molecule than the energy released from the hydroxylation. On the (010), (101) and (110) surfaces, OH fragments relaxed in a manner to allow simultaneous binding to two of the surface Zn cations, which is also reflected in the most negative hydroxylation adsorption energies of -0.672, -0.450, and -0.421 eV per water molecule, respectively. The weaker dissociative adsorption energies compared to the mole-cular water adsorption indicate that the overall dissociation process is endothermic, suggesting that water dissociation would not occur spontaneously on the different β-ZnP$_2$ sur-faces. The level of surface stabilisation upon hydroxylation is quantified through the hydroxylated surface energies and relaxation percentage as shown in Table 3, and it can be seen that the extent of surface stabilisation through a dissociated full monolayer of water is lower than that induced by the molecular water adsorption, Fig. 5a. This behaviour can be rationalised by considering the fact that molecular water binds more strongly to surface cation sites and provides a better

Fig. 6 Top and side views of low-Miller index surfaces of β-ZnP$_2$ with full coverage of water after dissociative adsorption (hydroxylation). Atomic colour: Zn in grey, P in peach, O in red, and H in white.

coordination of Zn atoms than the dissociated OH fragment. Consequently, progression of the γ_h for hydroxylated surfaces as a function of the chemical potential of water, Fig. 5b and c, indicates dissociative adsorption to be less likely observed on the surfaces in a humid environment.

Equilibrium Wulff morphology of β-ZnP₂ nanocrystals

Using the calculated relaxed, hydrated, and hydroxylated surface energies, the equilibrium Wulff morphologies of β-ZnP₂ under vacuum and full monolayer hydrated (molecular water) or hydroxylated (dissociated water) conditions were constructed, as shown in Fig. 7. Six out of the seven investigated low-Miller index surfaces appear in the equilibrium crystal morphology of β-ZnP₂ in vacuum, but the high surface stability of the (011) surface compared to the (111) surface hinders the appearance of the latter in the final morphology. Alongside the (011) surface, the low surface energies of the (001) and (100) surfaces induce the appearance of their large surface areas in the nanocrystal. Upon hydration, these three prominent surfaces all experience an increase in exposed areas but, owing to the very favourable adsorption of molecular water, the expansion is the greatest for the (010) surface, whereas the combination of higher surface energies and weaker water interaction causes the disappearance of the (110) and (101) surfaces from the hydrated crystal morphology.

Hydroxylation-induced morphology changes are less striking, which coincides with the decreased level of surface stabilisation compared to the hydration processes. The surface experiencing the most notable increase in surface area is again the (010) surface. Any changes in the appearances of the remaining five surfaces are minimal and they all remained present in the morphology, in contrast to the hydrated nanocrystal.

Charge transfers and electronic structure analysis

The incipient oxidation of β-ZnP₂ surfaces may be driven by the charge transfer process between the interacting surface species

and the adsorbing water molecules. A chemical picture was gained by characterising the changes in the Bader charge ($\Delta q = q_{\text{before\_adsorption}} - q_{\text{after\_adsorption}}$) of Zn binding sites and of the adsorbing water molecules, as summarised in Table 4 (molecular adsorption).

Generally, we found that the Bader charge of the interacting Zn site increased relative to the naked surface site, as reflected in the positive $\Delta q(\text{Zn})$ values. The positive $\Delta q(\text{Zn})$ values indicate that the interacting Zn sites undergo oxidation to some extent upon water adsorption. In most cases, the water molecules are reduced to a small extent upon molecular adsorption as reflected in their $\Delta q(\text{H}_2\text{O})$ values, Table 4. The level of oxidation of the Zn sites is found to increase with hydroxylation (dissociation), as reflected in the large positive $\Delta q(\text{Zn})$ values reported in Table 5. Similarly, the interaction of dissociated H atoms at P sites on the different surfaces caused P atoms to be significantly oxidised, becoming positively charged compared to their negative charge in the naked surfaces. The H atoms have gained a significant amount of charge ($>1\ e^-$ at all surfaces) from the interacting P sites, which caused them to undergo significant oxidation. The OH^- species have also gained significant negative charge from the interacting Zn sites, compared to molecular water, causing the Zn ions to be oxidised to a greater extent upon hydroxylation. Similarly to previous report on the Zn₃P₂ surfaces,[50] the significant amount of charge loss by the interacting surface atoms to the adsorbing H₂O, OH and H species is suggested as the primary origin of the initial oxidation of the β–ZnP₂ surfaces.

The effect of hydration or hydroxylation on the electronic work function, ϕ, which determines the photoemission properties of different β-ZnP₂ surfaces, was ascertained by computing the work function of each surface before (ϕ) and after full monolayer hydration (ϕ_h) and hydroxylation ($\phi_{h\text{-ox}}$), as summarised in Table 6. The ϕ of the unhydrated surfaces ranges from the lowest value of 4.139 eV for the (111) surface to the highest value of 4.614 eV for the (001) surface, which is
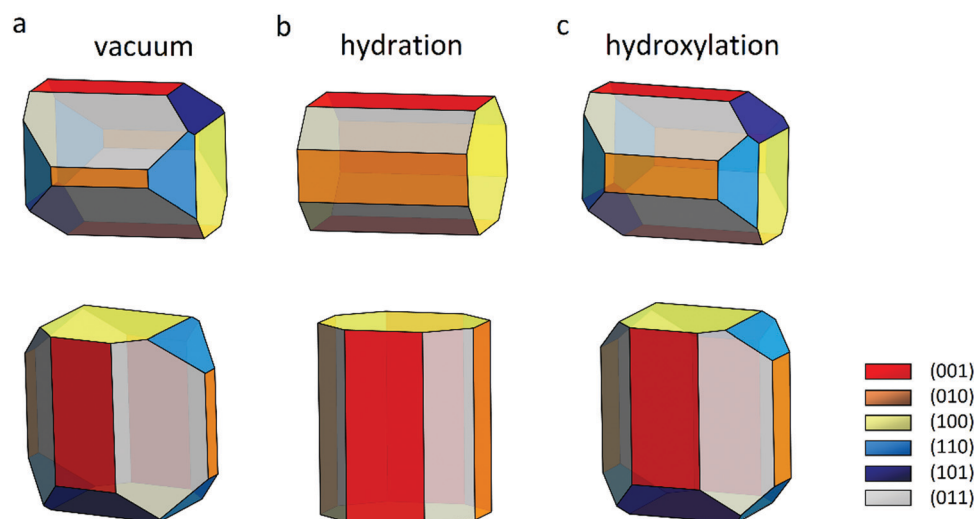

Fig. 7 Wulff morphologies of β-ZnP₂ (a) in vacuum, (b) after hydration, and (c) after hydroxylation.

Table 4 Changes in the Bader charge of water molecules after the molecular adsorption on the low-Miller index β-ZnP$_2$ surfaces and Zn atoms they are binding to

	mH$_2$O	Δq(Zn)/$|e^-|$	Δq(H$_2$O)/$|e^-|$
(001)	1 (Zn$_{in\text{-}plane}$)	+0.119	−0.013
	2	+0.077, +0.105	+0.004, −0.026
(010)	1 (Zn$_{in\text{-}plane}$)	+0.111	−0.020
	1 (Zn$_{channel}$)	+0.122	−0.019
	2	+0.071, +0.161	−0.030, −0.040
(100)	1 (Zn$_{in\text{-}plane}$)	+0.117	−0.006
	1 (Zn$_{channel}$)	+0.114	−0.011
	2	+0.101, +0.105	−0.013, −0.022
(011)	1 (Zn$_{in\text{-}plane}$)	+0.097	−0.006
	1 (Zn$_{channel}$)	+0.123	+0.001
	2	+0.089, +0.118	+0.003, −0.004
(101)	1 (Zn$_{in\text{-}plane}$)	+0.111	+0.004
	1 (Zn$_{channel}$)	+0.120	−0.008
	2	+0.108, +0.104	+0.026, +0.016
(110)	1 (Zn$_{channel}$)	+0.187	−0.006
	2	+0.279 (same atom adsorption)	−0.041, +0.005
(111)	1 (Zn$_{in\text{-}plane}$)	+0.099	−0.004
	1 (Zn$_{channel}$)	+0.156	−0.032
	2	+0.108, +0.165	−0.036, −0.030
	3	+0.091, +0.111, +0.157	−0.007, −0.038, −0.034

Table 5 Changes in the Bader charge of OH and H fragments of water molecules after the dissociative adsorption on the low-Miller index β-ZnP$_2$ surfaces and Zn/P atoms they are binding to

	mH$_2$O	Δq(Zn)/$|e^-|$	Δq(P)/$|e^-|$	q(OH)/$|e^-|$	q(H)/$|e^-|$
(001)	2	+0.256, +0.259	+1.382, +1.381	−1.637, −1.639	−1.143, −1.147
(010)	2	+0.215, +0.299	+1.310, +1.217	−1.638, −1.671	−1.169, −1.138
(100)	2	+0.247, +0.259	+1.292, +1.517	−1.625, −1.652	−1.220, −1.141
(011)	2	+0.223, +0.219	+1.285, +1.256	−1.652, −1.658	−1.112, −1.139
(101)	2	+0.238, +0.201	+1.215, +1.235	−1.619, −1.655	−1.106, −1.153
(110)	2	+0.237, +0.356	−0.043, +1.346	−1.659, −1.643	−1.198, −1.174
(111)	3	+0.216, +0.234, +0.337	+1.283, +1.124, +1.336	−1.639, −1.650, −1.638	−1.140, −1.133, −1.145

Table 6 Calculated work functions of the naked (ϕ) and full monolayer hydrated (ϕ_h) and hydroxylated ($\phi_{h\text{-}ox}$) β-ZnP$_2$ surfaces

	ϕ/eV	ϕ_h/eV	$\phi_{h\text{-}ox}$/eV
(001)	4.614	4.869	5.419
(010)	4.561	4.838	4.860
(100)	4.429	4.801	4.738
(011)	4.245	4.195	4.413
(101)	4.382	4.255	4.401
(110)	4.402	4.715	4.645
(111)	4.139	4.004	4.152

consistent with the fact that surfaces with denser packing of atoms tend to have higher work functions than those with more open lattices.[51] The low work functions predicted for bare β-ZnP$_2$ surfaces should facilitate electron emission and hence make them highly suitable for optoelectronic applications.

Relative to the bare surfaces, an increase in the work function of both the full monolayer hydrated and hydroxylated (001), (010), (100), and (110) surfaces is observed, Table 6. However, a reduction in the work function is predicted for the (011), (101), and (111) surfaces. The changes in the work function of the fully hydrated and unhydrated surfaces are between 0.05 and 0.37 eV, depending on the surface. Differences of a wider range of 0.01–0.81 eV were captured for the hydroxylated counterparts, alongside an increase in the work function captured for all seven surfaces. The changes in the work function may be ascribed to the observed electron transfers from the surface Zn atoms to the oxygen atoms of water molecules/OH fragments, resulting from differences in their electronegativity, where the intensity of charge exchange controlled by the orientation of adsorbates upon relaxation dictates the dipole generation and the work function alternations. In the case of molecular adsorption, multiple water molecules can either adsorb in the same orientation (e.g. the (011) surface with H atoms pointed towards the surface, leading to a decrease in the work function, or the (010) surface with H atoms positioned horizontal to the surface, resulting in an increased work function) or they can be facing in opposite directions (e.g. (001) and (101) surfaces, providing contrasting contributions to the dipole moment of the system), as seen for example of Pt surface work functions with oppositely oriented water layers.[52] When the water is dissociated, OH and H fragments both contribute to the charge reordering in O–Zn and H–P bonds, with OH fragments almost exclusively pointing away from the surface, which results in an amplified inward dipole moment and more pronounced increase in the work functions of hydroxylated surfaces. The hybridisation between the O p-states of the adsorbed water molecules and the
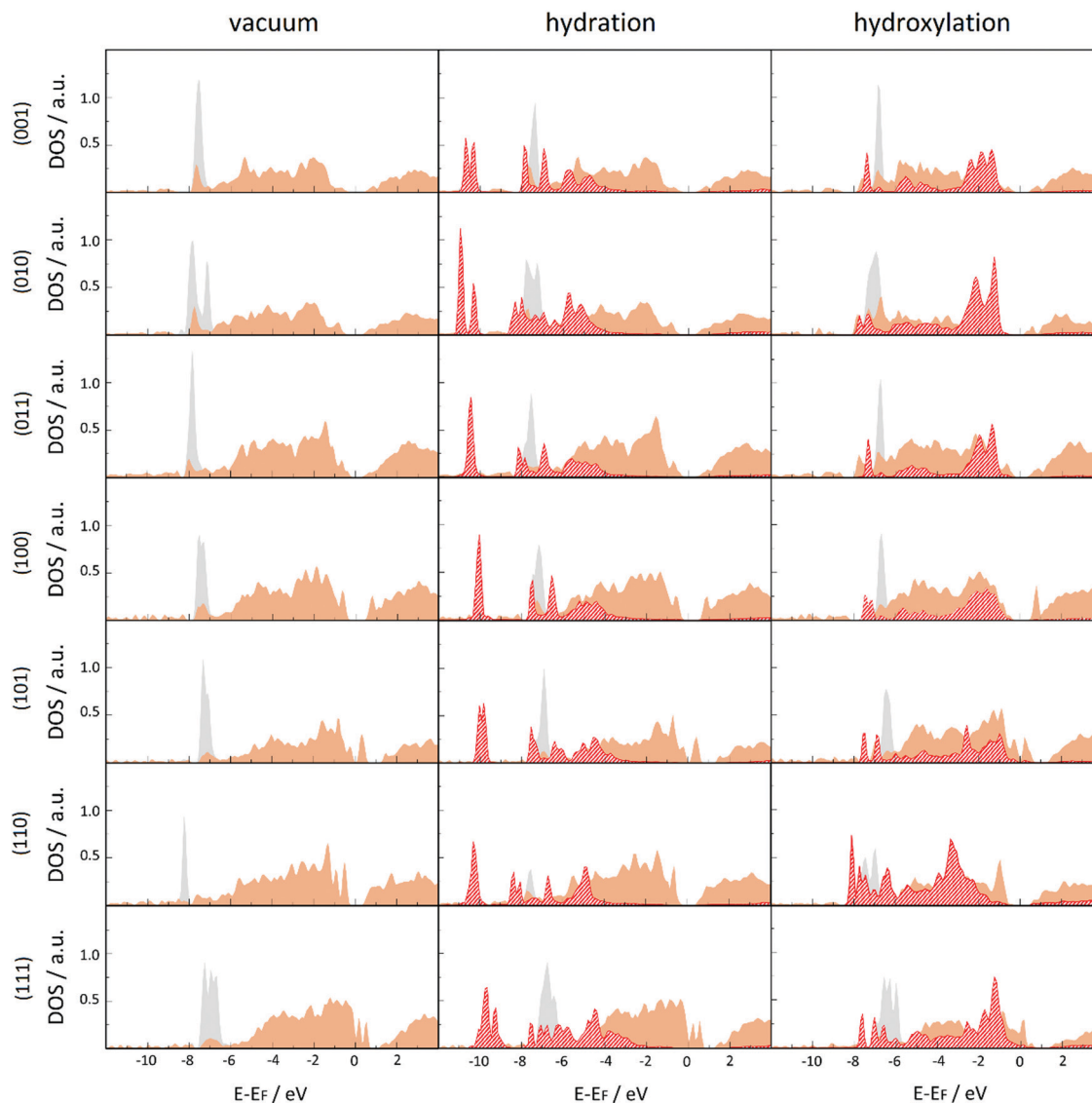
Fig. 8 Projected densities of state (DOS) for clean, hydrated, and hydroxylated β-ZnP$_2$ surfaces; Zn 3d orbitals in grey, P 2p orbitals in orange, and O 2p orbitals in red. Axes are the same for all the graphs. The occupancies have been scaled with respect to the number of atoms.

interacting surface Zn atoms induces changes in the electronic structure of the different surfaces. The effect of full monolayer coverage of molecularly or dissociatively adsorbed water on the electronic structures of β-ZnP$_2$ surfaces was ascertained by the predicted projected density of states (pDOS), as shown in Fig. 8. The main hybridisation peaks upon hydroxylation are obtained in the −1.0 to −3.0 eV range, whereas those upon hydration are found at much lower energies, starting at about −5.0 eV. Considering the initial positioning and orbital composition of valence and conduction bands of bare β-ZnP$_2$ surfaces, the DOS of monolayer hydrated and hydroxylated surfaces indicate minimal changes in those properties that are accountable for the nature and energy of the band gap. Hence, the semi-conducting characteristics of the β-ZnP$_2$ surfaces are found to be preserved upon both hydration and hydroxylation.

Conclusions

Periodic density functional theory calculations have been performed to systematically characterise the surface structures, composition, stabilities, morphology, and electronic properties of β-ZnP$_2$ low-Miller index surfaces under vacuum and hydrated/hydroxylated conditions. It was demonstrated from a thermodynamic point of view that water molecules will preferentially remain molecularly adsorbed on the β-ZnP$_2$ surfaces through their O atom at Zn sites, rather than to proceed with the dissociation and hydroxylation of the surfaces. The strength of water adsorption on each surface is found to decrease with the increasing number of water molecules. It is clear from our calculated surface energies that the molecular water adsorption (hydration) affects the stability of the β-ZnP$_2$ surfaces more than the dissociative water adsorption

This journal is © the Owner Societies 2021

Phys. Chem. Chem. Phys., 2021, 23, 26482–26493 | 26491

(hydroxylation), substantially modifying the equilibrium morphology of β-ZnP$_2$ nanocrystals. Bader charge analysis has revealed that the Zn sites to which H$_2$O and OH species are bound undergo facile oxidation, due to charge transfer to the adsorbing water or dissociated OH and H species. Due to oxidation of the different ZnP$_2$ surfaces, adsorption-induced changes were observed in the electronic work function and partial density of states. Our results provide a chemical picture of the hydration and hydroxylation processes, and the subsequent incipient oxidation of β-ZnP$_2$ surfaces in the presence of water. We suggest that efforts need to be made to passivate the surfaces of β-ZnP$_2$ nanoparticles or thin films, for example through *in situ* vapor-phase functionalisation with organic surfactants,[53,54] which can enhance their surface stability against oxidation in the presence of moisture.

Conflicts of interest

There are no conflicts to declare.

Acknowledgements

References

1 M. A. Green, Third generation photovoltaics: Solar cells for 2020 and beyond, *Phys. E*, 2002, **14**, 65–70.

2 G. Conibeer, Third-generation photovoltaics, *Mater. Today*, 2007, **10**, 42–50.

3 B. Parida, S. Iniyan and R. Goic, A review of solar photovoltaic technologies, *Renewable Sustainable Energy Rev.*, 2011, **15**, 1625–1636.

4 L. Wang, *et al.*, Tuning the p-type conductivity of ZnSe nanowires via silver doping for rectifying and photovoltaic device applications, *J. Mater. Chem. A*, 2013, **1**, 1148–1154.

5 J. H. Engel and A. P. Alivisatos, Postsynthetic doping control of nanocrystal thin films: Balancing space charge to improve photovoltaic efficiency, *Chem. Mater.*, 2014, **26**, 153–162.

6 S. Masudy-Panah, *et al.*, Titanium doped cupric oxide for photovoltaic application, *Sol. Energy Mater. Sol. Cells*, 2015, **140**, 266–274.

7 L. X. Shao, K. H. Chang and H. L. Hwang, Zinc sulfide thin films deposited by RF reactive sputtering for photovoltaic applications, *Appl. Surf. Sci.*, 2003, **212–213**, 305–310.

8 Y. Bi, Y. Yuan, C. L. Exstrom, S. A. Darveau and J. Huang, Air stable, photosensitive, phase pure iron pyrite nanocrystal thin films for photovoltaic application, *Nano Lett.*, 2011, **11**, 4953–4957.

9 Y. Wu, *et al.*, Synthesis and Photovoltaic Application of Copper (I) Sulfide Nanocrystals, *Nano Lett.*, 2008, **8**, 2551–2555.

10 J. Schrier, D. O. Demchenko, L. W. Wang and A. P. Alivisatos, Optical properties of ZnO/ZnS and ZnO/ZnTe heterostructures for photovoltaic applications, *Nano Lett.*, 2007, **7**, 2377–2382.

11 A. Živković, A. Roldan and N. H. de Leeuw, Density functional theory study explaining the underperformance of copper oxides as photovoltaic absorbers, *Phys. Rev. B*, 2019, **99**, 035154.

12 C. Wadia, A. P. Alivisatos and D. M. Kammen, Materials availability expands the opportunity for large-scale photovoltaics deployment, *Environ. Sci. Technol.*, 2009, **43**, 2072–2077.

13 E. A. Fagen, Optical properties of Zn$_3$P$_2$, *J. Appl. Phys.*, 1979, **50**, 6505–6515.

14 J. M. Pawlikowski, Absorption edge of Zn$_3$P$_2$, *Phys. Rev. B: Condens. Matter Mater. Phys.*, 1982, **26**, 4711–4713.

15 N. C. Wyeth and A. Catalano, Spectral response measurements of minority-carrier diffusion length in Zn$_3$P$_2$, *J. Appl. Phys.*, 1979, **50**, 1403–1407.

16 J. P. Bosco, S. B. Demers, G. M. Kimball, N. S. Lewis and H. A. Atwater, Band alignment of epitaxial ZnS/Zn$_3$P$_2$ heterojunctions, *J. Appl. Phys.*, 2012, **112**, 093703.

17 M. Bhushan, Schottky solar cells on thin polycrystalline Zn$_3$P$_2$ films, *Appl. Phys. Lett.*, 1982, **40**, 51–53.

18 V. V. Sobolev, A. I. Kozlov, Y. I. Polygalov, V. E. Tupitsyn and A. S. Poplavnoi, Reflectivity Spectra and Band Structure of the Zinc and Cadmium Diphosphides, *Phys. Status Solidi*, 1989, **154**, 377–388.

19 I. V. Bodnar, *et al.*, Photosensitive structure from the tetragonal modification of ZnP$_2$ single crystals, *J. Appl. Spectrosc.*, 2009, **76**, 220–226.

20 K. B. Aleynikova, A. I. Kozlov, S. G. Kozlova and V. V. Sobolev, Crystal Chemistry and Optical Properties of Monoclinic Zinc Diphosphide, *Mold. J. Phys. Sci.*, 2004, **3**, 137–148.

21 V. V. Sobolev and N. N. Syrbu, Optical Spectra and Energy Band Structure of the Monoclinic Crystals ZnP$_2$ and ZnAs$_2$, *Phys. Status Solidi*, 1972, **51**, 863–872.

22 I. S. Gorban, M. M. Bilyi, I. M. Dmitruk and O. A. Yeshchenko, Multiserial Structure of Excitonic Energy Spectrum in Monoclinic ZnP$_2$ Crystal, *Phys. Status Solidi*, 1998, **207**, 171–181.

23 K. Ito, Y. Matsuura, T. Nakazawa and H. Takenouchi, Photovoltaic Effect in Monoclinic ZnP$_2$, *Jpn. J. Appl. Phys.*, 1981, **20**, 109.

24 A. Živkovic, B. Farkaš, V. Uahengo, N. H. De Leeuw and N. Y. Dzade, First-principles DFT insights into the structural, elastic, and optoelectronic properties of α and β-ZnP₂: Implications for photovoltaic applications, *J. Phys.: Condens. Matter*, 2019, **31**, 265501.

25 M. Futsushara, K. Yoshioka and O. Takai, Degradation of Zn₃N₂ films prepared by reactive rf magnetron sputtering, *J. Korean Inst. Surf. Eng.*, 1996, **29**, 563–569.

26 M. Bär, *et al.*, Impact of air exposure on the chemical and electronic structure of ZnO:Zn₃N₂ thin films, *Appl. Phys. Lett.*, 2009, **94**, 012110.

27 F. J. Pern, *et al.*, Stability of TCO window layers for thin-film CIGS solar cells upon damp heat exposures, *Reliab. Photovolt. Cells, Modul. Components, Syst. II*, 2009, **7412**, 74120K.

28 T. P. Dhakal, *et al.*, Moisture-induced surface corrosion in AZO thin films formed by atomic layer deposition, *IEEE Trans. Device Mater. Reliab.*, 2012, **12**, 347–356.

29 E. Polydorou, *et al.*, Avoiding ambient air and light induced degradation in high-efficiency polymer solar cells by the use of hydrogen-doped zinc oxide as electron extraction material, *Nano Energy*, 2017, **34**, 500–514.

30 P. E. Blöchl, Projector augmented-wave method, *Phys. Rev. B: Condens. Matter Mater. Phys.*, 1994, **50**, 17953–17979.

31 G. Kresse and D. Joubert, From ultrasoft pseudopotentials to the projector augmented-wave method, *Phys. Rev. B: Condens. Matter Mater. Phys.*, 1999, **59**, 1758–1775.

32 W. Kohn and L. J. Sham, Self-consistent equations including exchange and correlation effects, *Phys. Rev.*, 1965, **140**, A1133.

33 P. Hohenberg and W. Kohn, Inhomogeneous Electron Gas, *Phys. Rev.*, 1964, **136**, B864–B871.

34 G. Kresse and J. Furthmüller, Efficient iterative schemes for ab initio total-energy calculations using a plane-wave basis set, *Phys. Rev. B: Condens. Matter Mater. Phys.*, 1996, **54**, 11169–11186.

35 J. P. Perdew, K. Burke and M. Ernzerhof, Generalized Gradient Approximation Made Simple, *Phys. Rev. Lett.*, 1996, **77**, 3865–3868.

36 S. Grimme, J. Antony, S. Ehrlich and H. Krieg, A consistent and accurate ab initio parametrization of density functional dispersion correction (DFT-D) for the 94 elements H-Pu, *J. Chem. Phys.*, 2010, **132**, 154104.

37 G. W. Watson, E. T. Kelsey, N. H. de Leeuw, D. J. Harris and S. C. Parker, Atomistic simulation of dislocations, surfaces and interfaces in MgO, *J. Chem. Soc., Faraday Trans.*, 1996, **92**, 433–438.

38 G. Wulff, XXV. Zur Frage der Geschwindigkeit des Wachsthums und der Auflösung der Krystallflächen, *Z. Kristallogr. - Cryst. Mater.*, 1901, **34**, 449–530.

39 R. V. Zucker, D. Chatain, U. Dahmen, S. Hagege and W. C. Carter, New software tools for the calculation and display of isolated and attached interfacial-energy minimizing particle shapes, *J. Mater. Sci.*, 2012, **47**, 8290–8302.

40 M. Chase, NIST-JANAF Thermochemical Tables, 4th Edition, *J. Phys. Chem. Ref. Data, Monogr.*, 1998, **9**, 1–1951.

41 Z. Yang, X. Wang, L. Liu, S. Yang and X. Su, Density functional theory studies on elastic and electronic properties of tetragonal ZnP₂, *Solid State Sci.*, 2011, **13**, 1604–1607.

42 I. E. Zanin, K. B. Aleinikova and M. Y. Antipin, Analysis of chemical bonding in the α and β modifications of zinc diphosphide from X-ray diffraction data, *Crystallogr. Rep.*, 2003, **48**, 199–204.

43 C. Manolikas, J. van Tendeloo and S. Amelinckx, The "devil's staircase" in CdP₂ and ZnP₂, *Phys. Status Solidi*, 1986, **97**, 87–102.

44 M. E. Fleet and T. A. Mowles, Structure of monoclinic black zinc diphosphide, ZnP₂, *Acta Crystallogr., Sect. C: Cryst. Struct. Commun.*, 1984, **40**, 1778–1779.

45 I. J. Hegyi, E. E. Loebner, E. W. Poor and J. G. White, Two crystal forms of ZnP₂, their preparation, structure, and optoelectronic properties, *J. Phys. Chem. Solids*, 1963, **24**, 333–337.

46 I. G. Stamov, N. N. Syrbu, V. V. Ursaki and A. V. Dorogan, Energy band structure and optical constants of ZnAs₂ crystals, *Opt. Commun.*, 2012, **285**, 3104–3110.

47 L. E. Soshnikov, V. M. Trukhan, T. V. Golyakevich and H. L. Soshnikova, Elastic and dielectric properties of AᴵᴵBⱽ₂ (A = Cd or Zn, B = P or As) single crystals, *Crystallogr. Rep.*, 2005, **50**, S37–S45.

48 V. Samuel and V. J. Rao, Optical and valence band studies of ZnP₂ thin films, *J. Mater. Res.*, 1989, **4**, 185–188.

49 H. M. Huang, Y. L. Li and Z. Zeng, Structural, elastic, and electronic properties of compressed ZnP₂, *Phys. B*, 2013, **419**, 112–115.

50 N. Y. Dzade, Unravelling the early oxidation mechanism of zinc phosphide (Zn₃P₂) surfaces by adsorbed oxygen and water: A first-principles DFT-D3 investigation, *Phys. Chem. Chem. Phys.*, 2020, **22**, 1444–1456.

51 J. Wang and S. Q. Wang, Surface energy and work function of fcc and bcc crystals: Density functional study, *Surf. Sci.*, 2014, **630**, 216–224.

52 A. Malek and M. H. Eikerling, Chemisorbed Oxygen at Pt(111): a DFT Study of Structural and Electronic Surface Properties, *Electrocatalysis*, 2018, **9**, 370–379.

53 L. Brockway, M. Van Laer, Y. Kang and S. Vaddiraju, Large-scale synthesis and in situ functionalization of Zn₃P₂ and Zn₄Sb₃ nanowire powders, *Phys. Chem. Chem. Phys.*, 2013, **15**, 6260–6267.

54 N. Y. Dzade, First-Principles Insights into the Interface Chemistry between 4-Aminothiophenol and Zinc Phosphide (Zn₃P₂) Nanoparticles, *ACS Omega*, 2020, **5**, 1025–1032.

This journal is © the Owner Societies 2021

Phys. Chem. Chem. Phys., 2021, **23**, 26482–26493 | **26493**